Applicability of Geographically Distributed Simulations

Mazheruddin Syed, *Member, IEEE*, Tran The Hoang, Alkistis Kontou, *Student Member, IEEE*, Alexandros Paspatis, *Member, IEEE*, Graeme Burt, *Member, IEEE*, Quoc Tuan Tran, *Senior Member, IEEE*, Efren Guillo-Sansano, Steffen Vogel, Ha Thi Nguyen, *Member, IEEE* and Nikos Hatziargyriou, *Life Fellow, IEEE*

Abstract—Geographically distributed simulations (GDS) overcome the inherent limitations in capabilities of single research infrastructure to accurately represent large-scale complex power and energy systems within representative operating environments in real-time. The feasibility of GDS has been proven, however, there is a lack of confidence in its adoption owing to limited evidence of its stability and accuracy that ascertain its practical applicability. This paper presents detailed small signal stability models for GDS setups with two interface signals transformations. The models have been validated by empirical analysis and used for determining the boundaries for stable operation of GDS setups. For the common region of stability of the two transformations considered, accuracy analysis presented offers insights for their selection. This advancement, thereby, enables realisation of experimental setups that can cater for the growing need to design and validate operational schemes that ensure robust and resilient operation of critical national infrastructure.

Index Terms—Accuracy, geographically distributed simulations (GDS), power hardware-in-the-loop (PHIL), stability.

I. INTRODUCTION

HARDWARE-in-the-loop has proven to be a valuable approach to accelerate the validation and deployment of novel technologies, with an increasing number of laboratories across the world adopting the approach [1]. The rapidly increasing complexity of power and energy systems (due to increased decentralization, decarbonization and digitalization) presents a challenge for single research laboratories, as existing capabilities (computational, expertise or equipment) will have to expand to encapsulate the growing complexity to ensure rigorous validation and roll-out of novel technologies at pace. This has encouraged the development and establishment of the concept of geographically distributed simulations (GDS), allowing for complementary expertise, additional equipment, domains and computational resources to be

M. Syed and G. Burt are with the Institute for Energy and Environment, University of Strathclyde, Glasgow, G1 1RD, UK. (e-mail: mazheruddin.syed@strath.ac.uk)

T. T. Hoang is with the French Alternative Energies and Atomic Energy Commission, France and the University of Danang, University of Science and Technology, Danang, Vietnam. (email: tran-the.hoang@cea.fr, htthe@dut.udn.vn)

A. Kontou, A. Paspatis and N. Hatziagyriou are with the Institute of Communication and Computer Systems, National Technical University of Athens, Athens, 157 80, Greece.

E. Guillo-Sansano is with Cooperativa Eléctrica Benéfica San Francisco de Asís, Alicante, 03330, Spain.

Q. T. Tran is with the French Alternative Energies and Atomic Energy Commission, France. (email: quoctuan.tran@cea.fr)

S. Vogel is with the Institute for Automation of Complex Power System, RWTH Aachen University, 52074 Aachen, Germany.

H. T. Nguyen is with the University of Connecticut, Storrs, CT 06269, United States.

harnessed across multiple laboratories that are geographically dispersed [2]. GDS involves the split of a power network into two or more subsystems for simulation at geographically dispersed laboratories. The subsystems are coupled over the internet, facilitated by low latency communications technologies and existing power hardware-in-the-loop (PHIL) interfaces. Some perceived benefits of GDS are summarized below, (not a comprehensive list of benefits):

- Comprehensive Characterization: Where the real-time simulation capability is limited due to computational constraints of the digital real time simulator, the simulators across multiple laboratories can be utilized to realize more detailed large scale models for high fidelity simulations. Examples of such experiments have been reported in [3], [4].
- Representative Systems: With the transition of our power system towards an integrated energy system with decarbonization of heat and transport, the concept of GDS allows for domain specific laboratories (such as heat and electrical power) to be interconnected to evaluate next generation concepts to facilitate the transition. Even within a domain, the equipment at each laboratory is unique and therefore the concept of GDS allows for utilization of hardware equipment of different laboratories within an experiment enabling the realization of broader range and more representative testing scenarios [5], [6].
- Acceleration of Validation: GDS supports the acceleration of validation in two ways:
(i) Enables integration of specialist skills and services such as in [7], where the communications emulation capability of one laboratory was utilized for an experiment by another laboratory, both geographically dispersed. This saves time and effort in realizing services that might be readily available for utilization.
(ii) Facilitates the cooperation between industrial partners as sensitive models are no longer required to be shared, can be run at independent organization facilities with only a data link to other cooperating organizations [8]. This adds an additional level of intellectual property protection and helps accelerate the validation. In terms of industrial partners developing controls, the GDS concept further enables the testing of prototype controllers without having to be delivered to a laboratory, making it logistically more convenient [9], [10].

GDS implementations have been reported across the world, spanning from a country [11] to multiple countries [12] to continents [7] - with the longest reported link being between USA and Australia (13,570 km) [13]. A comprehensive review of the technological advancements in GDS has been reported

in [14]. Although a promising approach that is gathering far reaching attention, its wide-scale adoption is hampered owing to limited understanding of its applicability.

As with PHIL simulations, the applicability of GDS is driven by the stability and accuracy of the setups. Stability and accuracy of PHIL setups have been extensively discussed in literature. PHIL setups are widely modeled as s-domain transfer functions that are subsequently utilized for stability analysis using Bode criterion [15], [16], Nyquist criterion [17] or Routh-Hurwitz criterion [18]–[20]. In [21], it was shown that the stability and accuracy of a PHIL setup is much influenced by the choice of interface algorithm, with a comparison of stability of commonly adopted interface algorithms presented in [22]. The impact of time delay on the stability of PHIL setups was discussed in [23]–[25], where deterioration in stability with increase in time delay was reported. In [19], the impact of power amplifier (switched mode) on the stability of PHIL setups was analyzed and concluded that the approximation of power amplifier as time delay in s-domain was inappropriate as the power amplification itself impacted the stability of the PHIL setup. A number of techniques to improve the stability of PHIL setups have been proposed, such as the addition of hardware inductance in [26], feedback current filtering in [27], shifting impedance method in [17], multi-rate partitioning in [28], multi-time-step transmission line interface in [29], use of open-loop inverter as power amplifier in [30], with a comparison of a few of these approaches ([17], [26]–[28]) presented in [31].

From a theoretical modelling perspective, there are three differences that can be drawn out between PHIL and GDS setups: (i) the GDS setups inherently incorporate larger time delays owing to the geographically dispersed nature of the setup, (ii) the GDS setups may or may not incorporate a power amplifier to interconnect the two subsystems, and (iii) the interface signals are transformed to DC quantities before their exchange in GDS. The s-domain transfer function models for PHIL setup can be extended for stability analysis of GDS setups - the model readily allows for integration of larger time delays and more often for simplicity the power amplifier is approximated as ideal for the analysis of stability [15], [21], [32]. However, the conventional transfer function models thus far used do not allow for the representation of the transformation of the interface signals. The interface signals in GDS are transformed as the exchange of signals as instantaneous time-domain quantities has been found to be inappropriate for GDS [4]. In addition, the transformation of the signals facilitates the incorporation of time delay compensation during the transformation of the signals back to time-domain quantities, an essential requirement for GDS due to the presence of larger inherent time delays. The transformations of signals has been more recently adopted for PHIL studies as well to realize more accurate setups incorporating time delay compensation [33], [34]. In [3], it was identified that the transformation of the interface signals impacts the stability of the GDS setup under consideration. The conventional simplified transfer function model was extended where the transformations were represented by the equivalent filters adopted for their implementation. Although a step forward, offering valuable insight of the impact of the transformations, further empirical

analysis have demonstrated limited suitability of that approach over representative time delays and varied system parameters.

There are currently no representative models available for stability analysis of PHIL simulations that utilize interface signal transformations or GDS. Furthermore, with more than one transformation available for realizing GDS setups (synchronous and asynchronous, explained in more detail in Section II), there is no literature available to offer practical guidance on the choice of transformation for the implementation of GDS setups. To address these gaps, in this paper, the stability and accuracy of GDS setups is investigated to establish its practical applicability. The key contributions of the paper are summarised below:

- The inability of existing simplified models to characterize the stability of GDS is demonstrated through a comparison with empirical simulation analysis. With no such analysis reported in literature, this paper is the first in offering the valuable insight that warrants the development of more accurate models for stability analysis of GDS.
- To remedy the lack of representative models for stability analysis of GDS with interface signals transformation, small signal stability models for two coupling interface transformation approaches, synchronous and asynchronous, have been developed . This will allow for accurate assessment of stability of GDS setups by the wider research community, and the developed models can be directly (or with minor modifications) adopted for accurate stability analysis of PHIL setups.
- Boundaries for stable operation of GDS for synchronous and asynchronous coupling have been established with respect to impedance ratio, time delay and hardware composition. This will enable prospective GDS user take an informed decision on the choice of coupling transformation for given application at hand.
- While accuracy of PHIL setups has been used as measure to communicate the confidence in simulations undertaken [35]–[37], this paper presents accuracy analysis of synchronous and asynchronous coupling in the common region of their stability. While the choice of coupling is obvious outside the common range of stability, accuracy analysis conducted in this paper with respect to change in voltage and frequency provides practical guidance in choice of coupling.

The remainder of the paper is organized as follows: Section II presents the fundamentals of the coupling interfaces. The suitability of conventional stability analysis is evaluated by means of comparison with empirical analysis in Section III. Models for accurate stability analysis for synchronously and asynchronously coupled GDS are derived in Section IV, followed by their validation and practical application discussed in Section V. The accuracy analysis of GDS setups with the two couplings is presented in Section VI followed by two GDS implementations for real-world smart-grid applications discussed in Section VII. Future research directions have been identified in Section VIII while Section IX concludes the paper.

II. COUPLING INTERFACES

The coupling of two subsystems, split for simulation across geographically distributed research infrastructures, is subject

(a) Synchronously coupled GDS
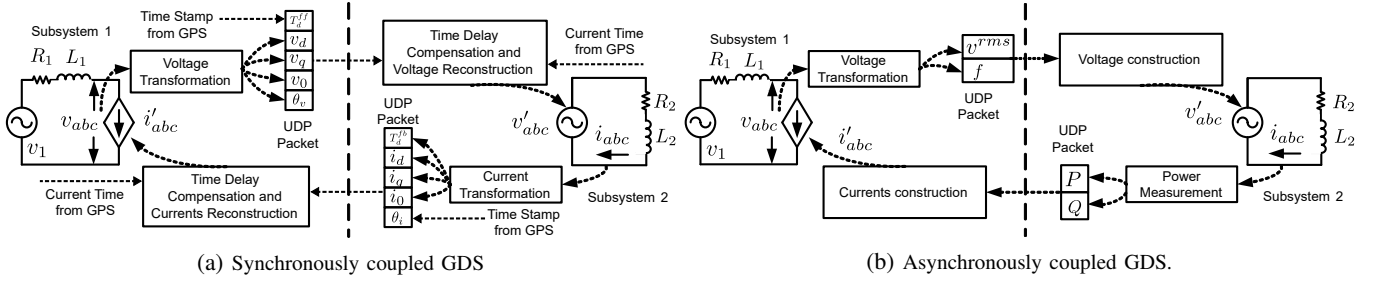
(b) Asynchronously coupled GDS.

Fig. 1: Synchronous and asynchronous GDS representations

to selection of a suitable coupling interface. A number of interface algorithms have been proposed in literature [22], this paper will adopt the voltage type ideal transformer model (V-ITM), where the voltage from Subsystem 1 PCC is reproduced at Subsystem 2 PCC by means of a controlled voltage source, while the currents in response to the reproduced voltage are fed back to Subsystem 1 PCC through a controlled current source. The V-ITM interface algorithm is a popular choice for PHIL and GDS setups owing to its ease of implementation. The choice of interface algorithm dictates the choice of interface signals, as such the chosen V-ITM requires the voltage signals from Subsystem 1 to be transferred to Subsystem 2 and the current signals to be transferred from Subsystem 2 to Subsystem 1. The exchange of interface signals as instantaneous time domain quantities has been shown to be inappropriate for packet based communications over the internet [4]. Therefore, a two step process of interface signal transformation (to DC quantities) before their transfer and signal reconstruction upon arrival is most commonly adopted for GDS implementations. This paper adopts two approaches presented in literature, namely the synchronous coupling approach using direct-quadrature (dq) transformation and the asynchronous coupling approach using root mean square (RMS).

A. Synchronous Coupling

A GDS setup adopting V-ITM interface algorithm and synchronous coupling is shown in Fig. 1a. In this approach, the three phase quantities (voltages in the feed-forward loop and currents in the feedback loop) are transformed into DC quantities (dq components). These DC quantities are transferred to the corresponding subsystem (to Subsystem 2 in feed-forward loop and to Subsystem 1 in feedback loop), where upon their receipt three phase quantities are reconstructed before further use. In addition to the dq components, the approach requires the transfer of $\theta = \omega t$ among the subsystems to enable accurate reproduction of the signals with time delay compensation. Therefore, the approach is also referred as synchronous coupling due to the fact that the two subsystems are synchronized with respect to time. The following subsections present the transformations in the feed-forward and feedback loop, followed by the details of time delay compensation employed.

1) Feed-forward Loop: Voltage signals from Subsystem 1 are transferred to Subsystem 2 in the feed-forward loop. First, the three phase voltages (v_a, v_b and v_c) are transformed to v_α and v_β using Clarke transformation, followed by their transformation to v_d and v_q using Park transformation as [38]

$$\begin{bmatrix} v_d \\ v_q \end{bmatrix} = \begin{bmatrix} \cos\theta & \sin\theta \\ -\sin\theta & \cos\theta \end{bmatrix} \begin{bmatrix} v_\alpha \\ v_\beta \end{bmatrix} \qquad (1)$$

where v_d and v_q are the direct and quadrature components of the voltage and θ is the phase angle of the voltage measured at Subsystem 1.

The two components with corresponding $\theta = \omega t$ are sent to Subsystem 2 over the internet using User Datagram Protocol (UDP). Upon receipt of the signals at Subsystem 2, the α, β, and γ components are obtained by applying the inverse Park transformation as, [38]

$$\begin{bmatrix} v'_\alpha \\ v'_\beta \end{bmatrix} = \begin{bmatrix} \cos\theta' & -\sin\theta' \\ \sin\theta' & \cos\theta' \end{bmatrix} \begin{bmatrix} v'_d \\ v'_q \end{bmatrix} \qquad (2)$$

where θ' is the compensated phase angle calculated as

$$\theta' = \theta + \Delta\theta = \theta + T_d^{ff} \cdot 2\pi f \qquad (3)$$

$\Delta\theta = T_d^{ff} \cdot 2\pi f$ is the additional phase angle added during the reconstruction of the signals to compensate for the feed-forward time delay T_d^{ff} [33]. More details on time delay compensation presented in Section II-A-3. The α, β, and γ components are then transformed to abc using the inverse Clarke transformation for injection at the PCC of Subsystem 2.

2) Feedback Loop: The current signals from Subsystem 2 are transferred to Subsystem 1 in the feedback loop. The current $dq0$ components (i_d, i_q and i_0) can be obtained from the instantaneous three phase currents (i_a, i_b and i_c) by using the Clarke-Park transformation as in the feed-forward loop. Then, upon receipt of the currents at Subsystem 1, the signals are reconstructed in a similar way as in the feed-forward loop. It should be noted that the phase compensation for the current phase angle is calculated by using the time delay of the feedback loop, i.e., T_d^{fb}.

3) Time Delay Compensation: Time delay compensation is paramount to the realization of GDS setups with synchronous coupling. The large inherent time delay due to geographical
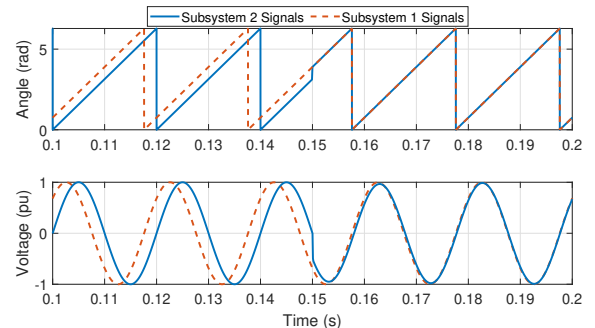

Fig. 2: Time delay compensation.

distance between the two research infrastructures can lead to significant inaccuracies. Time delay remains a concern for the fidelity of PHIL simulations but the typically smaller delay in order of microseconds (compared to milliseconds in GDS) leads to relatively minor inaccuracies.

For an AC signal, the time delay appears as a phase shift and can be compensated by addition of phase equal to the time delay calculated as $\Delta\theta = T_d \cdot 2\pi f$, where T_d is the time delay [33]. Consider Fig. 2, where the voltage and its phase from the two Subsystems in GDS are presented. The Subsystem 2 signals appear to be phase shifted in comparison to the signals from Subsystem 1, and this phase shift is associated to the time delay. This difference is phase causes erroneous calculation of active and reactive power at the PCC leading to the inaccuracies aforementioned. The addition of phase enables reproduction of the signal at Subsystem 2 in such a way that it is in phase with the signal at Subsystem 1 as shown in Fig. 2. This eliminates any discrepancies in calculation of active and reactive powers at the PCC.

Time delay can be calculated and compensated at each Subsystem every time step, i.e., in feed-forward and feedback loop or can be compensated in entirety at one of the Subsystems. The time delay in PHIL systems can be estimated and is typically a constant (minor variability as reported in [39]). However, due to the nondeterministic nature of communications over the Internet, the time delay in GDS can vary considerably. The accurate calculation of the time delay requires GPS (Global Positioning System) clocks at each of the research infrastructures. Each UDP packet is time stamped with time before it is sent to the corresponding research infrastructure. Upon receipt of the UDP packet, the time stamp is compared with current time to determine the time delay. The synchronized measurement ensures accuracy in order of nanoseconds.

B. Asynchronous Coupling

This approach presents a much simpler alternative to synchronous coupling, as shown in Fig. 1b and explained in the following subsections.

1) Feed-forward Loop: In case of asynchronous coupling, the RMS value and frequency of each phase of the three phase voltages are transferred from Subsystem 1 to Subsystem 2 in the feed-forward loop. Defining phase A voltage as $v_a(t) = V_{am}(t)\cos(2\pi f \cdot t)$, its RMS value can be calculated as

$$V_a^{rms}(t) = \frac{\sqrt{2}}{T_w}\int_{t-T_w}^{t} v_a(t)\cos(2\pi f \cdot t)dt \qquad (4)$$

where T_w is the window lenwhere T_w is the window length of the RMS value computation at time instant t.gth of the RMS value computation at time instant t. Upon receipt of the RMS values and frequencies at Subsystem 2, the AC quantities are reconstructed as

$$v_a'(t) = V_a^{rms'}(t)\cos(2\pi f' \cdot t) \qquad (5)$$

where $V_a^{rms'}$ and f' are the RMS voltage and frequency received at Subsystem 2.
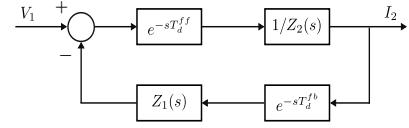

Fig. 3: SISO representation of PHIL setup.

2) Feedback Loop: As the two subsystems are not synchronised with respect to time, the currents from Subsystem 2 cannot be utilized for injection at Subsystem 1. Instead, the active and reactive powers measured at Subsystem 2 are transferred to Subsystem 1, where upon their receipt the currents for injection are calculated with reference to the PCC voltage at Subsystem 1 as

$$i_d(t) = \frac{3}{2}\frac{P'v_d - Q'v_q}{v_d^2 + v_q^2}, \quad i_q(t) = \frac{3}{2}\frac{P'v_q + Q'v_d}{v_d^2 + v_q^2} \qquad (6a,b)$$

The three phase currents i_a', i_b', and i_c' can be calculated using inverse Park and inverse Clarke transformation. However, it should be noted that the feedback loop of asynchronous coupling utilises the phase angle of the voltage at Subsystem 1 PCC (θ_v) instead of requiring the transfer of the phase angle of currents from Subsystem 2 and does not include the additional phase term to compensate for the time delay.

C. Security of Communications

GDS require the transmission of data between the research infrastructures involved over the Internet. Securing the transmission of data is essential as the experimental data can be sensitive in nature or due to the fact that the data can be driving hardware equipment at the research infrastructures that can be vulnerable to manipulation of data. There are two ways reported in literature in which the risk due to cyber-attacks is mitigated: (i) use of VPN (Virtual Private Network) or by utilizing software libraries that offer encryption and (ii) adding data check upon receipt of signals. The incorporation of features to secure the data transmission adds additional delays, but yields comparable performance given the large inherent delays involved. A summary of such approaches has been presented in [3].

III. CONVENTIONAL STABILITY ANALYSIS

In this section, the suitability of conventional stability analysis for synchronous and asynchronous GDS is evaluated. First, the model conventionally adopted for stability analysis is presented followed by theoretical and empirical evaluation of stability.

A. Modelling

The conventional approach to modelling a PHIL setup for stability analysis involves its representation as a single input single output (SISO) system. The simplified SISO representation of a PHIL setup is presented in Fig. 3. The fundamental difference between PHIL setup and GDS setup is the lack of power amplifier as interface between the two Subsystems considered and larger time delays due to the fact that the two Subsystems are geographically apart. However, as can be observed from Fig. 3, the conventional modelling approach

approximates the power amplifier behaviour as ideal (transfer function representation as unity) and therefore the same SISO is also applicable for the analysis of GDS setups. The open-loop transfer function of GDS setup can be defined as

$$G_{OL}(s) = \frac{Z_1(s)e^{-s \cdot 2T_d}}{Z_2(s)} \tag{7}$$

where $Z_1(s)$ and $Z_2(s)$ are the equivalent impedances of Subsystem 1 and Subsystem 2 respectively, with the time delay for the feed-forward loop as T_d^{ff} and feedback delay as T_d^{fb}. Assuming $T_d^{ff} \approx T_d^{fb}$, the total time delay of the setup is considered as $2T_d$.

B. Theoretical Analysis

The stability of the GDS setups can be evaluated theoretically by means of Nyquist stability criterion where poles of the closed-loop system are determined, equivalent to the zeros of the two characteristic equations [28]

$$1 + G_{OL}(s) = 0 \tag{8}$$

$$det(\mathbf{I} + \mathbf{G}_{OL}(s)) = 0 \tag{9}$$

where $\mathbf{I}$ is the dimension identity matrix. The impact of impedance ratio, time delay and power factor (PF) is presented in the following sub-sections.

1) Impact of Impedance Ratio Z_1/Z_2: The stability assessment for a range of Z_1/Z_2 (PF $= 0.95$, $T_d = 25$ ms) is shown in Fig. 4a. The Z_1/Z_2 boundary for stability is found as 1 with the system encircling -1 for any value of $Z_1/Z_2 > 1$.

2) Impact of Time Delay: The stability of GDS for T_d in range of 10-500 ms (PF $= 0.95$, $Z_1/Z_2 = 0.9$) is shown in Fig. 4b. From the conventional analysis it can be concluded that the T_d does not impact the stability of the GDS setups.

3) Impact of PF: The impact of PF on the stability of GDS setups with $Z_1/Z_2 = 0.4$ and $Z_1/Z_2 = 0.9$ ($T_d = 25$ ms) is shown in Fig. 4c and 4d. The decrease in PF tends to move the system towards instability, the impact is more significant as the Z_1/Z_2 approaches its stability boundary.

C. Empirical Analysis

This sub-section presents the empirical evaluation of stability conducted by means of simulations in MATLAB/Simulink. The results of analysis for synchronous and asynchronous coupling are presented in Fig. 5 and Fig. 6, respectively.

The first obvious distinction is the difference in results obtained for synchronous and asynchronous couplings. The simplified model adopted for stability analysis does not cater for the impact of coupling incorporated.

1) Impact of Impedance Ratio Z_1/Z_2: It is evident that the impedance ratio boundary for GDS setups is different for the two couplings and much smaller than the value derived from the conventional stability analysis. The Z_1/Z_2 boundary for synchronous coupling ($T_d = 25$ ms, PF $= 0.95$) is obtained as 0.2 (as in Fig. 5a) and 0.25 for asynchronous coupling (as in Fig. 6a).

2) Impact of Time Delay: The results for stability analysis with respect to time delay for synchronous coupling for $Z_1/Z_2 = 0.2$ and $Z_1/Z_2 = 0.6$ are presented in Fig 5b and 5c respectively, while the corresponding results for asynchronous coupling are presented in Fig. 6b and 6c respectively. In all the cases the PF is equal to 0.95. For $Z_1/Z_2 = 0.2$, the stability of synchronous coupling tends to instability with increase in time delay (unstable for $T_d > 25$ ms) while the stability of asynchronous coupling is not impacted by the time delay. For $Z_1/Z_2 = 0.6$, the stability boundary (with respect to T_d) for synchronous coupling has reduced to 4 ms, while the asynchronous coupling is unstable for any value of T_d considered.

3) Impact of PF: The conventional theoretical analysis of impact of PF on stability of GDS setups complies with the empirical analysis. The results for synchronous coupling for $Z_1/Z_2 = 0.05$ and $Z_1/Z_2 = 0.2$ are presented in Fig 5d and 5e respectively, while the corresponding results for asynchronous coupling are presented in Fig. 6d and 6e respectively. As can be observed, with decrease in PF the system tends towards instability with much significant impact as the Z_1/Z_2 reaches its stability boundary.

D. Discussion

The theoretical stability analysis of the simplified models identify a larger range of impedance ratio over which the GDS setups are stable, this is in direct contradiction to the empirical results where much smaller impedance ratio boundaries have been identified for both the couplings analysed. The simplified model also fails to identify the impact of time delay on the stability of GDS when not operating at the impedance ratio boundary of stability. Although the simplified model presents the same trend when analysing the impact of PF on the stability of GDS, the results do not match the empirical results quantitatively. The discrepancy between the theoretical and empirical analysis results is evident, highlighting the inability of the existing simplified model to accurately characterize the stability of GDS employing synchronous or asynchronous coupling. The evaluation of stability of GDS setup before its implementation is imperative to ensure a secure experimental run, particularly when hardware is involved. Erroneous results
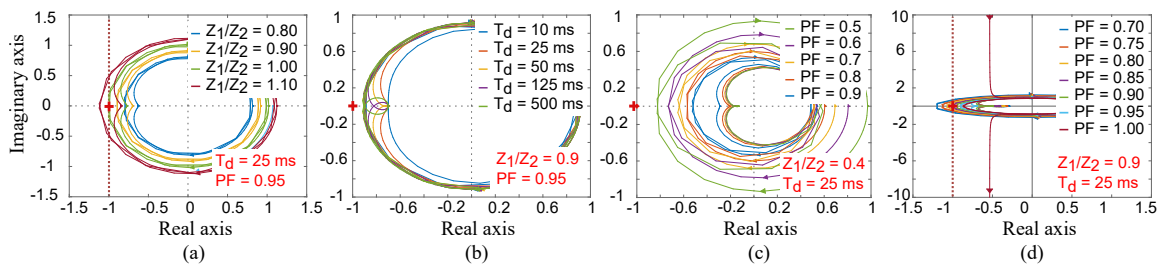

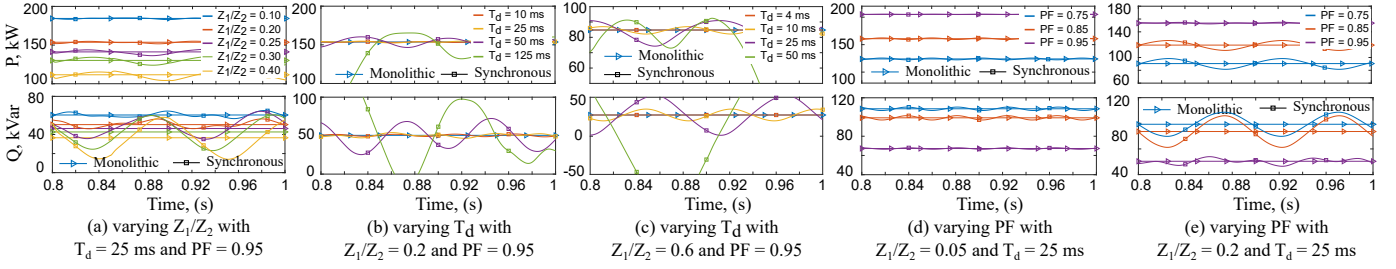Fig. 4: Nyquist plots based on the conventional method

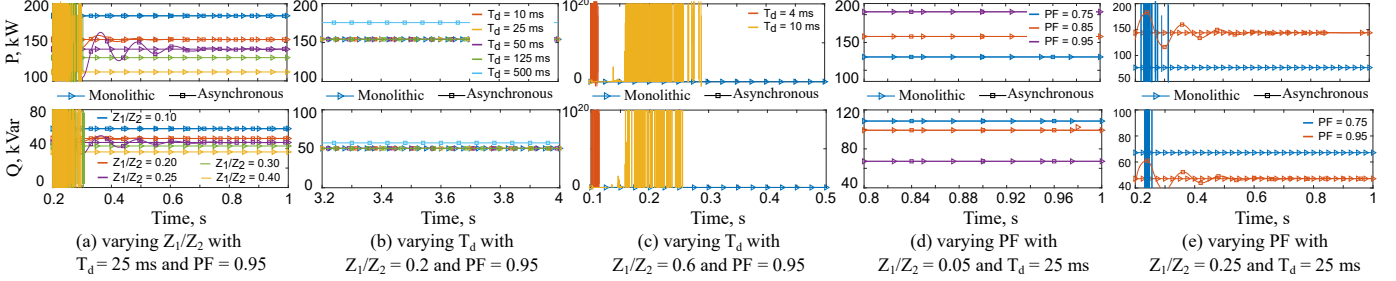Fig. 5: Empirical analysis for synchronous coupling

Fig. 6: Empirical analysis for asynchronous coupling

can lead in expense of time in realizing setups that are infeasible and/or damage to hardware equipment involved. This is the first of its kind evaluation, offering valuable insight that warrants the development of more accurate models that can accurately characterize the stability of GDS setups.

IV. MODELS FOR ACCURATE STABILITY ANALYSIS

In this section, accurate models for a synchronously and asynchronously coupled GDS setups are derived using small-signal stability analysis principle. Any state variable u of a dynamic system can be decomposed into two components, as

$$u = \bar{U} + \hat{u} \tag{10}$$

where $\bar{U}$ is the steady-state component and $\hat{u}$ is the small-signal variation component. Using this assumption, any non-linear system can be linearised around a steady-state operating point for stability analysis using linear systems theory. In the following subsections, open-loop transfer functions for synchronous and asynchronous GDS setups will be developed for accurate stability analysis.

A. Synchronous Coupling Model

The s-domain block diagram of the synchronously coupled GDS setup is illustrated in Fig. 7.

As discussed in section II-A1, the three phase voltages at the PCC in Subsystem 1 are transformed to v_α and v_β followed by their transformation to v_d and v_q. By application of small-signal theory as in (10) and neglecting the steady-state components with approximations ($\sin\hat{\theta} \approx \hat{\theta}$, $\cos\hat{\theta} \approx 1$), the relationships of the small-signal components of voltages between $\alpha\beta$ and dq frames can be obtained as

$$\begin{bmatrix} \hat{v}_d(t) \\ \hat{v}_q(t) \end{bmatrix} = \begin{bmatrix} \hat{v}_\alpha \cos\bar{\Theta} - \bar{V}_\alpha \hat{\theta} \sin\bar{\Theta} + \hat{v}_\beta \sin\bar{\Theta} + \bar{V}_\beta \hat{\theta} \cos\bar{\Theta} \\ \hat{v}_\beta \cos\bar{\Theta} - \bar{V}_\beta \hat{\theta} \sin\bar{\Theta} - \hat{v}_\alpha \sin\bar{\Theta} - \bar{V}_\alpha \hat{\theta} \cos\bar{\Theta} \end{bmatrix} \tag{11}$$

where $\hat{v}_\alpha$, $\bar{V}_\alpha$ are the small signal and steady state components of v_α respectively, $\hat{v}_\beta$ and $\bar{V}_\beta$ are the small signal and steady-state components of v_β respectively, and $\bar{\Theta}$ and $\hat{\theta}$ are the steady-state and small-signal components of the phase-angle of the voltage at PCC.

The positive sequence (PS) and negative sequence (NS) components can be obtained by application of Euler's formulas and Laplace transformation to (11) as

$$\begin{bmatrix} \hat{v}_d^+(s) \\ \hat{v}_d^-(s) \end{bmatrix} = \begin{bmatrix} \frac{1}{2}\hat{v}_\alpha - \frac{j}{2}\hat{v}_\beta + \frac{1}{2}\left(j\bar{V}_\alpha + \bar{V}_\beta\right)\hat{\theta} \\ \frac{1}{2}\hat{v}_\alpha + \frac{j}{2}\hat{v}_\beta + \frac{1}{2}\left(-j\bar{V}_\alpha + \bar{V}_\beta\right)\hat{\theta} \end{bmatrix} \tag{12}$$

$$\begin{bmatrix} \hat{v}_q^+(s) \\ \hat{v}_q^-(s) \end{bmatrix} = \begin{bmatrix} -\frac{j}{2}\hat{v}_\alpha + \frac{1}{2}\hat{v}_\beta - \left(\frac{1}{2}\bar{V}_\alpha + \frac{j}{2}\bar{V}_\beta\right)\hat{\theta} \\ \frac{j}{2}\hat{v}_\alpha + \frac{1}{2}\hat{v}_\beta + \left(-\frac{1}{2}\bar{V}_\alpha + \frac{j}{2}\bar{V}_\beta\right)\hat{\theta} \end{bmatrix} \tag{13}$$

where $\hat{v}_d^\pm(s)$ and $\bar{v}_q^\pm(s)$ are the small-signal quantities of the PS and NS components of v_d and v_q in s-domain, respectively.

Upon receipt of the dq components of the voltage at Subsystem 2, v_α' and v_β' can be reconstructed using inverse Park transformation (as explained in section II-A1). Employing the small-signal principle and neglecting the steady-state quantity
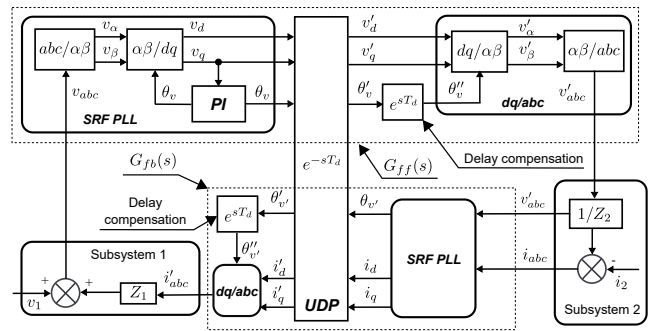

Fig. 7: Block diagram of the synchronous GDS in s-domain

in q frame, the relationship can be expressed as

$$
\begin{bmatrix} \hat{v}'_\alpha \\ \hat{v}'_\beta \end{bmatrix} = \begin{bmatrix} \frac{1}{2}\left(\hat{v}'^-_d + \hat{v}'^+_d\right) + \frac{j}{2}\bar{V}_d(\hat{\theta}''^- - \hat{\theta}''^+) + \frac{j}{2}\left(\hat{v}'^-_q - \hat{v}'^+_q\right) \\ \frac{-j}{2}\left(\hat{v}'^-_d - \hat{v}'^+_d\right) + \frac{1}{2}\bar{V}_d(\hat{\theta}''^- + \hat{\theta}''^+) + \frac{1}{2}\left(\hat{v}'^-_q + \hat{v}'^+_q\right) \end{bmatrix}
$$
(14)

Assuming time delay compensation of the PCC phase-angle is fully achieved, i.e. $\theta'' = \theta$, the α and β components of the voltage at Subsystem 2 can be represented by those received from Subsystem 1 as

$$
\begin{bmatrix} \hat{v}'_\alpha(s) \\ \hat{v}'_\beta(s) \end{bmatrix} = \begin{bmatrix} \hat{v}_\alpha e^{-sT^{ff}_d} + \bar{V}_\beta e^{-sTd^{ff}}\hat{\theta} + \frac{j}{2}\bar{V}_d(\hat{\theta}^- - \hat{\theta}^+) \\ \hat{v}_\beta e^{-sT^{ff}_d} - \bar{V}_\alpha e^{-sTd^{ff}}\hat{\theta} + \frac{1}{2}\bar{V}_d(\hat{\theta}^- + \hat{\theta}^+) \end{bmatrix}
$$
(15)

where T^{ff}_d is the time delay for the feed forward User Datagram Protocol (UDP) communication channel. As indicated in [40], the PS and NS components of the phase angle θ can be expressed by $\alpha\beta$ components of voltages as

$$
\begin{bmatrix} \hat{\theta}^- \\ \hat{\theta}^+ \end{bmatrix} = \begin{bmatrix} T^-_{PLL}\left(-j\hat{v}_\alpha + \hat{v}_\beta\right) \\ T^+_{PLL}\left(j\hat{v}_\alpha + \hat{v}_\beta\right) \end{bmatrix}
$$
(16)

where

$$
T^{+/-}_{1PLL} = \frac{G^{+/-}_{PLL}}{1 + \bar{V}_d G^{+/-}_{PLL}}
$$
(17)

$$
G^{+/-}_{PLL}(s) = G_{PLL}(s) = \left(k_p + \frac{k_i}{s}\right)\frac{1}{s}
$$
(18)

with G_{PLL} as the transfer function of the PLL block. By substituting (16) into (15) and assuming $T^-_{PLL} = T^+_{PLL} = T_{PLL}$, $\theta = \frac{1}{2}(\theta^- + \theta^+)$, the final expression for the transfer function of the feed-forward path, denoted by $G^{dq}_{ff}(s)$, can be obtained as

$$
G^{dq}_{ff}(s) = \begin{bmatrix} k_{v1} & k_{v2} \\ k_{v3} & k_{v4} \end{bmatrix}
$$
(19)

where

$$
k_{v1} = e^{-sT_d} + \bar{V}_d T_{PLL}, \quad k_{v2} = \bar{V}_\beta e^{-sT_d} T_{PLL}, \quad \text{(20a,b)}
$$

$$
k_{v3} = 0, \quad k_{v4} = e^{-sT_d} + \bar{V}_d T_{PLL} - \bar{V}_\alpha T_{PLL} e^{-sT_d}
$$
(20c,d)

Same approach can be applied to derive the transfer function of the feedback path. By analysis of the block diagram in Fig 7, the expressions describing the relationship between the α and β components of the currents at Subsystem 1 and Subsystem 2 are defined by

$$
\begin{bmatrix} \hat{i}'_\alpha(s) \\ \hat{i}'_\beta(s) \end{bmatrix} = \begin{bmatrix} \hat{i}_\alpha e^{-sT_d} + \bar{I}_\beta e^{-sTd} T_{PLL}\hat{v}_\beta + \bar{I}_d T_{PLL}\hat{v}_\alpha \\ \hat{i}_\beta e^{-sT_d} - \bar{I}_\alpha e^{-sTd} T_{PLL}\hat{v}_\beta + \bar{I}_d T_{PLL}\hat{v}_\beta \end{bmatrix}
$$
(21)

Substituting $\hat{v}_\alpha$ and $\hat{v}_\beta$ by $\hat{i}_\alpha$ and $\hat{i}_\beta$ through power relation, the final equation for the transfer function of the feedback path denoted by $G^{dq}_{fb}(s)$ can be represented as

$$
G^{dq}_{fb}(s) = \begin{bmatrix} k_{i1} & k_{i2} \\ k_{i3} & k_{i4} \end{bmatrix}
$$
(22)

where the coefficients in the equation of $G^{dq}_{fb}(s)$ remain the same as of $G^{dq}_{ff}(s)$. The compact form of the open loop transfer function for the synchronously coupled GDS setup depicted in Fig. 7 can be expressed as

$$
G^{dq}_{OL}(s) = G^{dq}_{ff}(s) \cdot G^{dq}_{fb}(s) \cdot \frac{Z_1(s)}{Z_2(s)}
$$
(23)

B. Asynchronous Coupling Model

The expression for calculation of the RMS value of the phase A voltage over a moving window of length T_w is presented in (4). By differentiating both sides and applying small-signal principle, the equation can be rewritten as

$$
\dot{v}^{rms}_a(t) = \frac{1}{\sqrt{2}}\left[\hat{v}_a(t)\cos\omega_0 t - \bar{v}_a(t - T_w)\cos\omega_0(t - T_w)\right]
$$
(24)

Applying Laplace transform to (24), the expression for the small-signal component of the RMS value of phase A voltage in s-domain is described by

$$
\hat{v}^{rms}_a(s) = \frac{1}{\sqrt{2}T_w s}(1 - e^{-sT_W})\left[\hat{v}^-_a + \hat{v}^+_a\right]
$$
(25)

Once the RMS values of the voltage arrives at Subsystem 2, the instantaneous voltage signal can be reconstructed as

$$
v'_a(t) = V^{rms'}_a(t)\cos(2\pi f't) = V^{rms'}_a(t)\cos(\omega' t)
$$
(26)

The small-signal quantity of $v'_a(t)$ is found as

$$
\hat{v}'_a(t) = -\hat{\theta}'\bar{V}^{rms'}\sin\bar{\Theta} + \hat{v}^{rms'}_a(t)\cos\bar{\Theta}
$$
(27)

where $\bar{V}'_{rms}$ is the steady-state quantity of the RMS value of phase A voltage. Applying Euler's equations and Laplace transform to expression of $v'_a(t)$

$$
\hat{v}'_a(s) = -\frac{\bar{V}^{rms}}{2j}(\hat{\theta}'^- - \hat{\theta}'^+) + -\frac{1}{2}(\hat{v}^{rms'-}_a + \hat{v}^{rms'+}_a)
$$
(28)

Equations describing NS component $\hat{v}^{rms'-}_a(s)$ and PS component $\hat{v}^{rms'+}_a(s)$ can be approximated from (25) as

$$
\hat{v}^{rms'\pm}_a(s) = \frac{1 - e^{-sT_d}}{\sqrt{2}T_d(s \pm j\omega_0)}\hat{v}_\alpha
$$
(29)

By substituting (16) into (28) and then the resulted expression into (29), the relationship between the α component of the voltages in the feed-forward path between two subsystems in Fig. 8 can be described as

$$
\hat{v}'_\alpha(s) = \sqrt{\frac{3}{2}}\left[G_1(s) + G_2(s)\right]\hat{v}_\alpha
$$
(30)

where

$$
G_1(s) = e^{-sT_d}\bar{V}^{rms}T_{PLL}
$$
(31)

$$
G_2(s) = e^{-sT_d}\frac{1 - e^{-sT_w}}{\sqrt{2}T_w}\frac{s}{s^2 + w_0^2}
$$
(32)

Using the same procedure, the β component of the voltage reproduced at Subsystem 2 can be defined by

$$
\hat{v}'_\beta = \sqrt{\frac{3}{2}}G_2(s)\hat{v}_\beta
$$
(33)

By using the Clark transformation, the equations for the three-phase voltages obtained at Subsystem 2 are defined by

$$
\hat{v}'_a(s) = \sqrt{\frac{3}{2}}\left[G_1(s) + G_2(s)\right]\hat{v}_\alpha
$$
(34)

$$
\hat{v}'_b(s) = \left(G_1 - \frac{1}{2}G_2\right)\hat{v}_\alpha(s) + \frac{\sqrt{3}}{2}G_2\hat{v}_\beta(s)
$$
(35)

$$
\hat{v}'_c(s) = \left(G_1 - \frac{1}{2}G_2\right)\hat{v}_\alpha(s) - \frac{\sqrt{3}}{2}G_2\hat{v}_\beta(s)
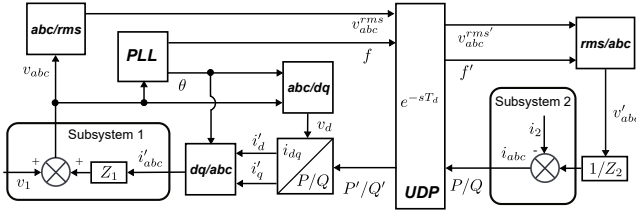$$
(36)

Fig. 8: Asynchronously coupled GDS block diagram in s-domain

A difference between synchronous and asynchronous coupling at this stage is that the latter uses the powers for closing the loop instead of currents. The measured powers can be determined through the three-phase currents and voltages at the Subsystem 2 as

$$p(t) = v'_a i_a + v'_b i_b + v'_c i_c \tag{37}$$

$$q(t) = \frac{1}{\sqrt{3}} \left[(v'_b - v'_c) i_a + (v'_c - v'_a) i_b + (v'_a - v'_b) i_c \right] \tag{38}$$

where i_a, i_b, and i_c are three-phase currents at Subsystem 2.

Employing small-signal principle for (37) and (38) and combining with (34), (35), and (36) provides

$$\hat{p}(s) = \left[\bar{I}^{rms} + \frac{\bar{V}^{rms}}{Z_2(s)} \right] (-G_1 + 2G_2) \hat{v}_\alpha \tag{39}$$

$$\hat{q}(s) = 0 \tag{40}$$

where $\bar{I}_{rms}$ is the steady-state component of the RMS value of the current at Subsystem 2. When the values of the measured powers reach Subsystem 1, the dq components of the current are calculated by

$$\hat{i}'_d(s) = \frac{2}{3} \frac{\hat{p}'(s)}{\bar{V}_d} = G_3(s) \hat{v}_\alpha, \quad \hat{i}'_q(s) = \frac{2}{3} \frac{\hat{q}'(s)}{\bar{V}_d} = 0 \tag{40a,b}$$

where

$$G_3(s) = \frac{2e^{-sT_d}}{3\bar{V}_d} \left[\bar{I}^{rms} + \frac{\bar{V}^{rms}}{Z_2(s)} \right] (-G_1 + 2G_2) \tag{41}$$

Finally, similar to (21), with some approximations, the small-signal quantities in s-domain of the $\alpha\beta$ components of the three-phase currents fed to the current source in Subsystem 1 is computed by using the inverse Park transformation with the phase angle derived from the phase angle of the voltage at Subsystem 1 PCC, i.e. θ in Fig. 8

$$\begin{bmatrix} \hat{i}'_\alpha(s) \\ \hat{i}'_\beta(s) \end{bmatrix} = \begin{bmatrix} \hat{i}'_d(s) + \frac{j}{2} \bar{I}_d (\hat{\theta}^- - \hat{\theta}^+) \\ \frac{1}{2} \bar{I}_d (\hat{\theta}^- + \hat{\theta}^+) \end{bmatrix} \tag{42}$$

Referring to (16) and (40a,b), it can be observed that the equations of the α and β components of the reconstructed currents in (42) incorporate dynamics of two different subsystems, one coming from the current reconstructed from the powers sent from Subsystem 2 and one from the phase angle of the voltage at Subsystem 1 PCC. The use of (34) to (36) to represent the dynamics of Subsystem 2, i.e. $\hat{i}'_d(s)$ in (40a,b), through those of Subsystem 1, i.e. $\hat{v}_\alpha(s)$ and $\hat{v}_\beta(s)$, enables obtaining the final expressions of the reconstructed currents as

$$\begin{bmatrix} \hat{i}'_\alpha(s) \\ \hat{i}'_\beta(s) \end{bmatrix} = \begin{bmatrix} G_3 + \bar{I}_d T_{PLL} & 0 \\ 0 & \bar{I}_d T_{PLL} \end{bmatrix} \begin{bmatrix} \hat{v}_\alpha \\ \hat{v}_\beta \end{bmatrix} \tag{43}$$

The open-loop transfer function of the asynchronously coupled GDS setup as in Fig. 8 can be represented as

$$G_{OL}^{rms}(s) = \begin{bmatrix} G_3 + \bar{I}_d T_{PLL} Z_2 & 0 \\ 0 & \bar{I}_d T_{PLL} Z_2(s) \end{bmatrix} \tag{44}$$

V. DETAILED STABILITY ANALYSIS

The objectives of this section are two-fold: (i) to validate the small-signal models developed in Section IV, and (ii) to determine the boundaries of stability for GDS setups.

A. Small Signal Model Validation and Analysis

In this section, the small-signal models developed for GDS setups with synchronous and asynchronous coupling are validated by means of an extended analysis with respect to impedance ratio, time delay and power factor.

1) Impact of Impedance Ratio: The impedance ratio is varied from 0.1 to 0.4 in steps of 0.05 while the time delay ($T_d = 25$ ms) and power factor (PF= 0.95) are kept constant. The Nyquist plots for the two coupling interfaces, synchronous (23) and asynchronous (44) are presented in Fig. 9a. The general trend of stability is in line with conventional analysis, i.e., with increase in impedance ratio the GDS setups tend towards instability. The stability margins derived from the proposed detailed models is in alignment with the empirical analysis, identified as 0.2 for synchronously coupled GDS setups and 0.25 for asynchronously coupled GDS setups.

2) Impact of Time Delay: The Nyquist plots for varying time delay from 10 ms to 125 ms with $Z_1/Z_2 = 0.15$ and PF = 0.95 are shown in Fig. 9b. In accordance with the empirical analysis, the setups with synchronous and asynchronous couplings are immune to variation in T_d for the Z_1/Z_2 considered. Furthermore, the suitability of the proposed models is also verified for setup with $Z_1/Z_2 = 0.6$, where the results obtained are in alignment with those obtained through the empirical analysis, i.e., the stability boundary (with respect to T_d) for synchronous coupling reduced to 4 ms, while the asynchronous coupling is unstable for any value of T_d considered (Fig. 5c and Fig. 6c vs Fig. 9c).

3) Sensitivity to Power Factor: The analysis from the developed models complies with the conventional and empirical analysis presented in Section III. The results for GDS setup with synchronous coupling for Z_1/Z_2 equal to 0.15 and 0.2 and asynchronous coupling for Z_1/Z_2 equal to 0.2 and 0.25 are presented in Fig 9d and 9e. As can be observed, with decrease in PF the system tends towards instability with much noticeable impact as the Z_1/Z_2 reaches its stability boundary.

B. Boundary Conditions and Practical Applications

In this subsection, the stability boundaries for synchronously and asynchronously coupled GDS setups are derived. With the general trend of impact of impedance ratio, time delay and power factor of the system under consideration on stability presented in previous subsection, here a comprehensive stability analysis within a practical range for identified parameters has been undertaken: $Z_1/Z_2 = [0.1, 1]$, $T_d = [500\,\mu s, 0.5\,s]$ and PF= [0.5, 1]. The derived boundary conditions are presented in Fig. 10, with Fig 10a presenting boundaries for synchronously coupled GDS setups while Fig. 10b presents boundaries for
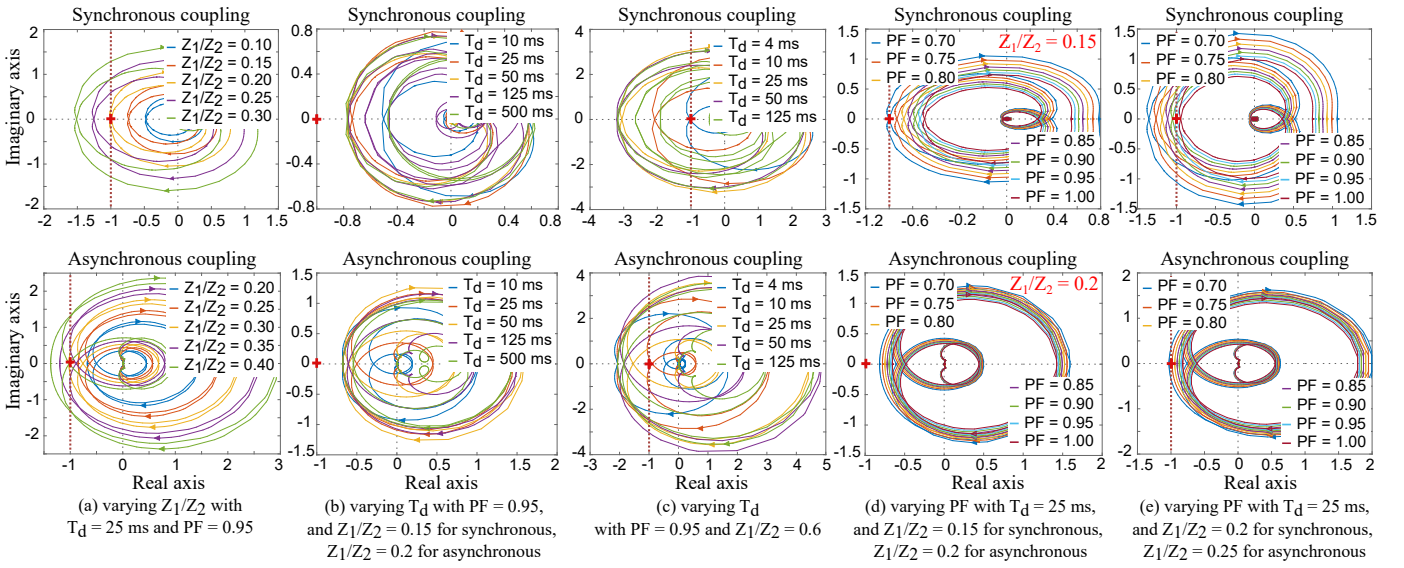
(a) varying Z_1/Z_2 with $T_d = 25$ ms and PF = 0.95

(b) varying T_d with PF = 0.95, and $Z_1/Z_2 = 0.15$ for synchronous, $Z_1/Z_2 = 0.2$ for asynchronous

(c) varying T_d with PF = 0.95 and $Z_1/Z_2 = 0.6$

(d) varying PF with $T_d = 25$ ms, and $Z_1/Z_2 = 0.15$ for synchronous, $Z_1/Z_2 = 0.2$ for asynchronous

(e) varying PF with $T_d = 25$ ms, and $Z_1/Z_2 = 0.2$ for synchronous, $Z_1/Z_2 = 0.25$ for asynchronous

Fig. 9: Nyquist plots based on the proposed stability models

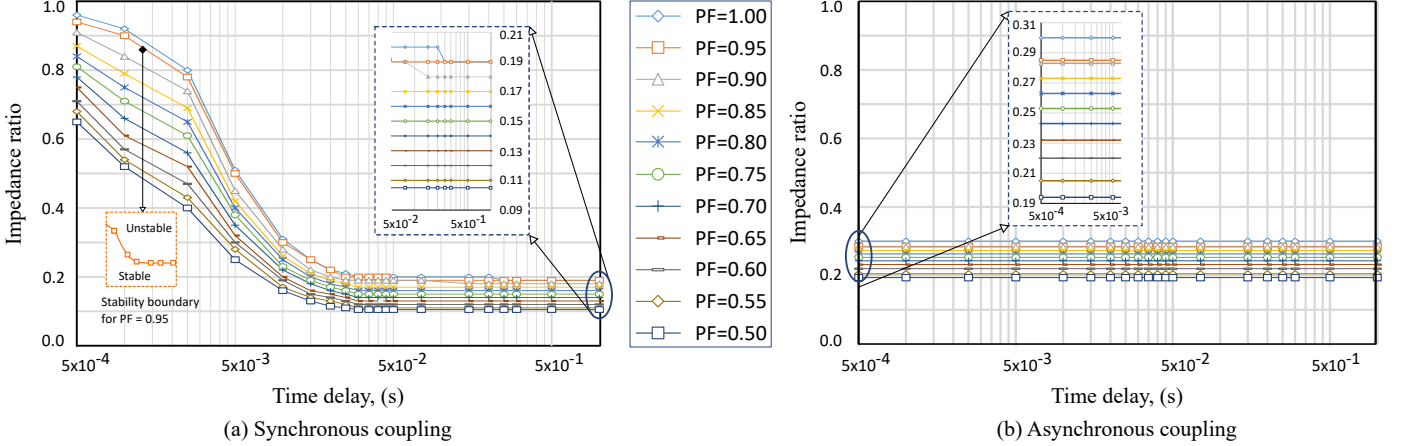(a) Synchronous coupling

(b) Asynchronous coupling

Fig. 10: Stability boundary conditions for GDS setups

asynchronously coupled GDS setups. The y-axis of the plot represents the impedance ratio plotted against logarithmic scale of time delay on x-axis. Each curve represents a given PF, with area under the curve representing stable region of operation. From the analysis it can be concluded that

- For synchronously coupled GDS setups, the stability is dominated by time delay, i.e., the time delay of a given setup determines the impedance ratio of systems that can be studied using GDS. A setup with time delay of $500\,\mu$s can be utilized for studies of systems with impedance ratio less than 0.95, however, this falls drastically to an impedance ratio of ~ 0.2 for any time delay greater than ~ 20 ms.
- The stability of asynchronously coupled GDS is dominated by impedance ratio of the setups and is not impacted by time delay. The impedance ratio limit for asynchronously coupled GDS is identified as ~ 0.3.
- A decreasing power factor generally reduces the impedance ratio limit for any given impedance ratio and time delay (compared to unity power factor).

From an application point of view, a synchronously coupled GDS setup is an obvious choice for systems with impedance ratio greater than 0.3, while respecting corresponding time delay and power factor boundaries depicted. For setups with impedance ratio between 0.15 and 0.3, the choice of coupling

needs careful consideration with respect to PF and time delay of the setup. For setups with impedance ratio less than 0.1, both synchronous and asynchronous coupling present good stability for the practical range of PF and time delay considered, a broader consideration of the accuracy of the setup should be in scope.

VI. ACCURACY ANALYSIS

In this section, the accuracy of interface coupling for GDS setups at the PCC is evaluated. Choosing appropriate metrics for comparison is essential. Two metrics have been defined to quantify the accuracy of the interface coupling as

- Maximum Instantaneous Power Tracking Error (MIPTE) is defined as the maximum excursion of the measured apparent power $S''(t)$ of the GDS setup compared to the measured apparent power $S'(t)$ of the monolithic setup.

$$\text{MIPTE} = \max\left(\frac{S'(t) - S''(t)}{\text{RMS}(S'(t))}\right) \qquad (45)$$

- Cumulative Power Tracking Error (CPTE) is defined as the sum of the tracking errors at every time step T_s from the application of disturbance to the time when measured

apparent power is restored within the tolerance band, i.e., for period of T_r.

$$\text{CPTE} = \frac{\sum_{k=0}^{N} (S'[k] - S''[k])}{\text{RMS}(S'(t))} \tag{46}$$

where $N = T_r/T_s$, with T_s as the time step. T_r is the error restoration time defined as the time elapsed from the disturbance initiation to when the measured apparent power returns and stays within the defined tolerance band ϵ.

$$T_r = \text{argmin}\{T_r \in \mathcal{R} \mid \forall\, t > T_r : \epsilon^+ < S''(t) < \epsilon^-\} \tag{47}$$

A smaller CPTE corresponds to better set point tracking capability.

In comparison to metrics in [37], the chosen metrics present a single value (analogous to cross-sectional evaluation as opposed to time-series) encapsulating the performance of the chosen interface. The MIPTE provides a measure of maximum instantaneous error of a given interface while CPTE captures its average performance over a given period of time.

The accuracy will be evaluated with respect to the same three parameters: time delay, impedance ratio and power factor. To allow for a fair comparative accuracy analysis of the two couplings, the range of parameters have been chosen such that both coupling interfaces are stable, obtained from Fig 10 as $Z_1/Z_2 = [0.05, 0.15]$, $T_d = [1\,\text{ms}, 100\,\text{ms}]$ and PF$= [0.75, 1]$. The remainder of this section will present the results of the comparison with respect to two disturbances, one step down in frequency (50 Hz to 49 Hz) followed by a step up in voltage (400 V to 440 V).

The results for the accuracy analysis for step change in frequency are presented in Fig. 11, with MIPTE for variation in parameters in Fig. 11a-11c and CPTE for variation in parameters in Fig. 11d-11f. As can be observed, the synchronous coupling exhibits an approximately linear trend where the accuracy deteriorates with increase in T_d, Z_1/Z_2 and decrease in PF. For all the variations in parameters considered, the asynchronous coupling presents better accuracy performance with minimal variation in accuracy with respect to the variations in parameters considered.

Likewise, the calculations of MIPTE and CPTE, which are obtained from step change in voltage, are shown in Fig. 12a-12c and Fig. 12d-12f, respectively. Generally it can be stated that synchronous coupling exhibits better accuracy when compared to asynchronous coupling for a step change in voltage. MIPTE is minimally impacted by T_d, higher Z_1/Z_2 exhibits lower MIPTE while lower PF exhibits higher MIPTE. Although the MIPTE is minimally impacted with variation in T_d, it can be observed that CPTE increases with increase in time delay (exhibiting exponential increase for the boundary of observation $T_d = 100\,\text{ms}$ and $Z_1/Z_2 = 0.15$. Similar to the analysis for step change in frequency, the accuracy for both the couplings deteriorates with decrease in PF.

VII. Case Studies

This section presents two case studies where GDS implementations for real-world smart grid applications have been realized. The use of the analysis conducted and presented within the previous subsections guides the choice of interface coupling, demonstrating support in applicability and implementation of GDS setups between research infrastructures.

A. Voltage Support in a Distribution Network

This section presents an example of GDS implementation for voltage control study within a distribution network. The distribution network under consideration is shown in Fig. 13, and has been adapted based on [41]. Each bus within the network comprises a mix of loads and Photovoltaic (PV) systems, represented in aggregation for simplicity. The objective of the study is to understand the capability of the battery energy storage system (BESS) to respond to voltage variations
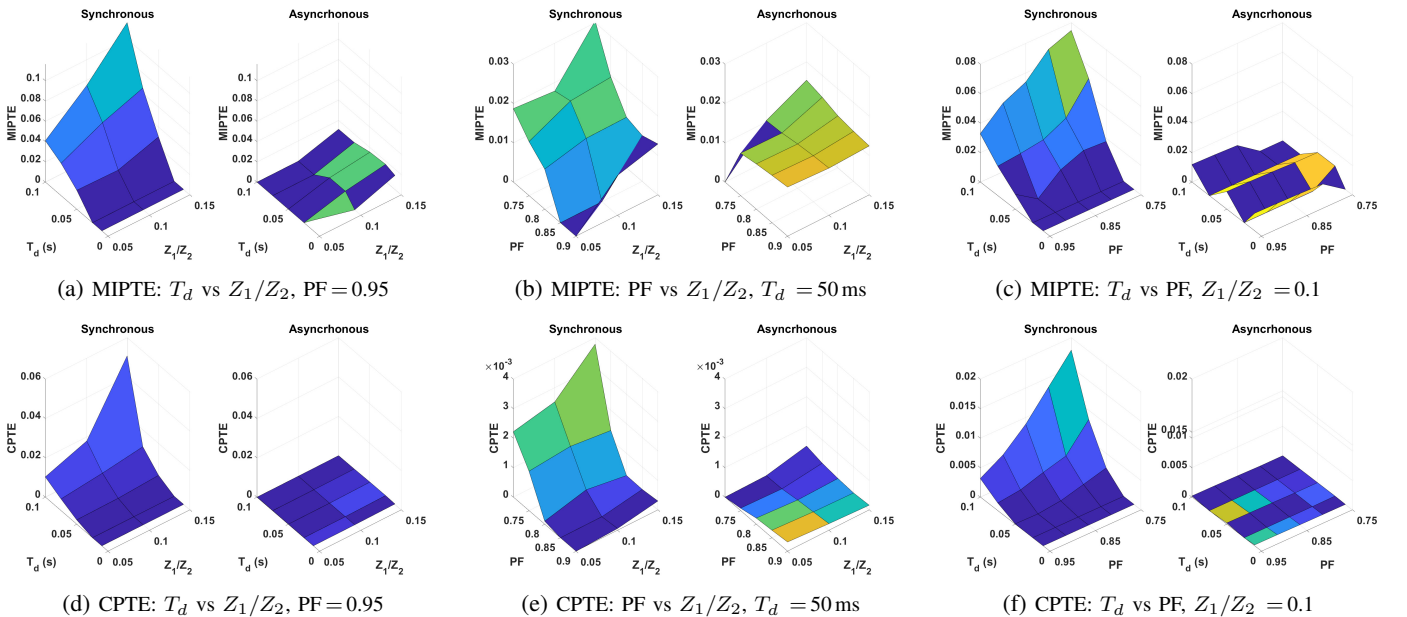

(a) MIPTE: T_d vs Z_1/Z_2, PF $= 0.95$ (b) MIPTE: PF vs Z_1/Z_2, $T_d = 50\,\text{ms}$ (c) MIPTE: T_d vs PF, $Z_1/Z_2 = 0.1$

(d) CPTE: T_d vs Z_1/Z_2, PF $= 0.95$ (e) CPTE: PF vs Z_1/Z_2, $T_d = 50\,\text{ms}$ (f) CPTE: T_d vs PF, $Z_1/Z_2 = 0.1$
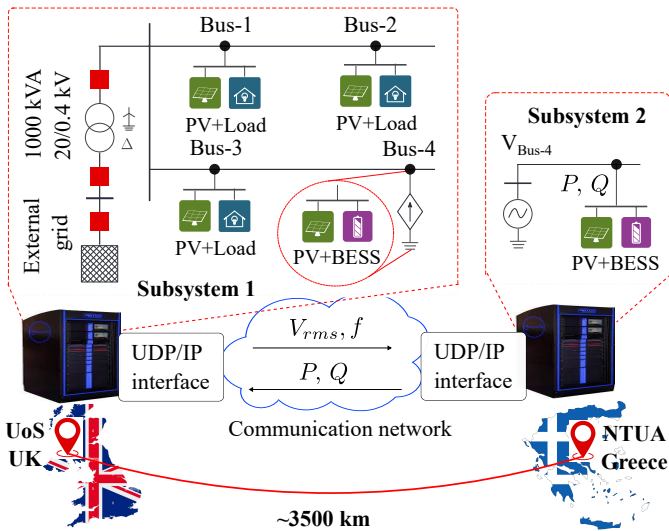
Fig. 11: Accuracy characterisation for step change in frequency

Fig. 13: Example asynchornous GDS setup between DPSL (UK) and EESL (Greece) for voltage support study in a distribution network.

Fig. 14: Results from example implementation of asynchronous GDS demonstrating voltage support in a distribution network.

and thereby supporting voltage regulation of the distribution network.

The two laboratories in consideration for the experiment are the Dynamic Power systems Laboratory (DPSL) at the University of Strathclyde (UoS) and the Electric Energy System Laboratory (EESL) at the National Technical University of Athens (NTUA), with a geographical distance of $\sim$3,500 km between the two. The average time delay between the two laboratories is $\sim$60 ms as shown in Fig. 14 (top), with maximum delay observed as $\sim$75 ms. The next step in implementation requires the evaluation of the equivalent impedance ratio at the PCC. The BESS can be integrated at any of the four buses within the distribution network, given the objective of testing the capability of the BESS to respond to variations in voltage.

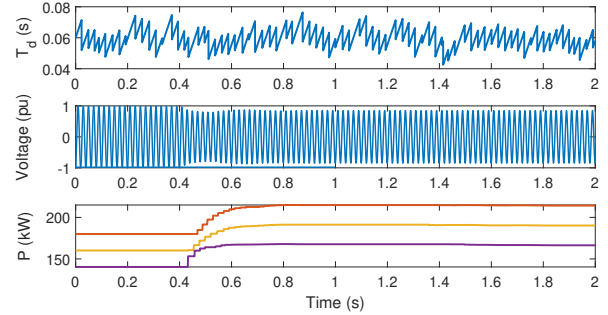With the inherent time delay and impedance ratio at hand,

an informed decision on choice of coupling can be made. The synchronous coupling is on the verge of stability for delays greater than $\sim$10 ms for $Z_1/Z_2 = 0.2$, and unstable for $Z_1/Z_2 = 0.3$ and $Z_1/Z_2 = 0.4$ (as in Fig. 10). The stability of asynchronous coupling is not dependant upon the time delay, while the coupling can remain stable for $Z_1/Z_2 = 0.2$ and $Z_1/Z_2 = 0.3$. While the synchronous coupling offers better accuracy for changes in voltage (as shown in Fig. 12), the asynchronous coupling offers wider range of scenarios for evaluation and therefore is a better choice for GDS implementation.

As shown in Fig. 13, the distribution network is simulated in a DRTS at DPSL (Subsystem 1) while the components at the bus are simulated in DRTS at EESL (Subsystem 2). With asynchronous coupling adopted for implementation, the rms voltage and frequency are sent from DPSL to EESL, while the active and reactive power in response to the voltage is sent from EESL to DPSL. To test the response of the BESS, a 10 % voltage step (reduction from 1 pu to 0.9 pu as in Fig. 13 (middle)) is introduced within Subsystem 1 by means of the on-load tap changer at the grid coupling

(a) MIPTE: T_d vs Z_1/Z_2, PF = 0.95

(b) MIPTE: PF vs Z_1/Z_2, T_d = 50 ms

(c) MIPTE: T_d vs PF, Z_1/Z_2 = 0.1

(d) CPTE: T_d vs Z_1/Z_2, PF = 0.95

(e) CPTE: PF vs Z_1/Z_2, T_d = 50 ms
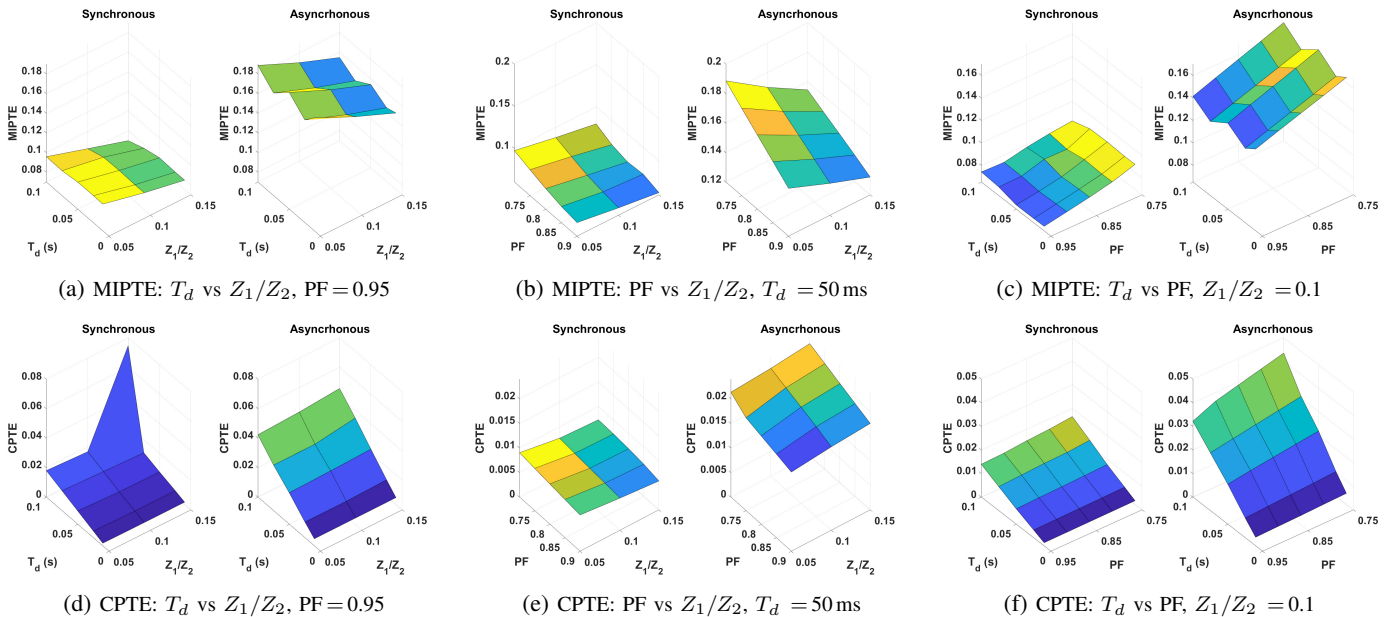
(f) CPTE: T_d vs PF, Z_1/Z_2 = 0.1

Fig. 12: Accuracy characterisation for step change in voltage
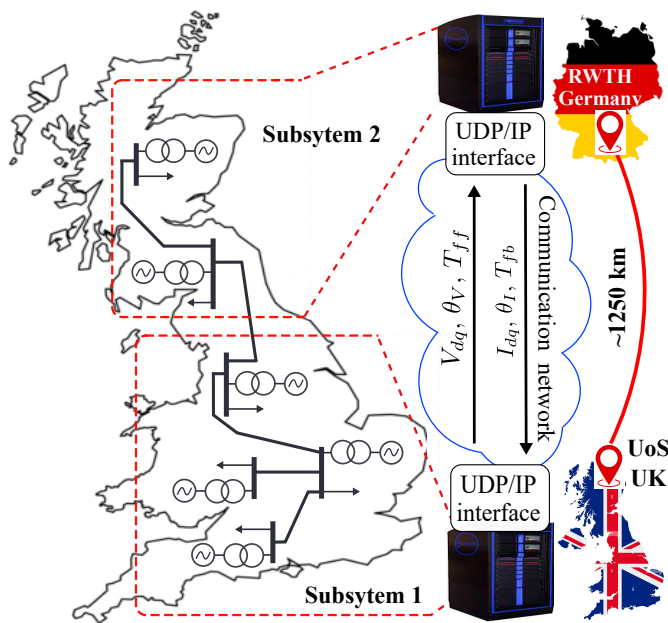
Fig. 15: Example synchronous GDS setup between DPSL (UK) and RTLab (Germany) for frequency support study in a transmission network.

Fig. 16: Results from example implementation of synchronous GDS demonstrating frequency support in a distribution network

point. BESS is rated at $100\,$kW and is designed to respond to variations in voltage by injecting active power. The combined response of the Subsystem 2 is presented in Fig. 13 (bottom). The response emulating three different impedance ratios has been presented, practically representative of different locations within the distribution network.

The transmission rate chosen for the implementation was varied with reported results from an exchange of interface signals at $100\,$Hz. As is evident, a successful implementation has been realized at much lower transmission rate than required for synchronously coupled GDS setups. This presents an additional advantage that can lead to increased adoption of GDS in circumstances where hardware capabilities are limited.

B. Frequency Support in a Transmission Network

This section presents an example GDS implementation for frequency control within a transmission network. A reduced six bus dynamic model of the Great Britain (GB) power network is considered, where each bus comprises an aggregated load and an aggregated generation unit. The generation units are synchronous generators modeled to reproduce the representative dynamics of GB power system. The objective of the study is the integration of inertial response (IR) through controllable loads within the network to support the frequency regulation.

In addition to the aforementioned laboratories (DPSL and EESL), the Real-Time Laboratory (RTLab) at RWTH Aachen University, Germany, is considered for the frequency control study. RTLab and DPSL are separated over a geographical distance of $\sim 1250\,$km. The average time delay between the two research infrastructures is $\sim 16\,$ms, with maximum observed delay of $\sim 28\,$ms as shown in Fig. 16 (top). An empirical evaluation has identified an impedance ratio $Z_1/Z_2 = 0.15$
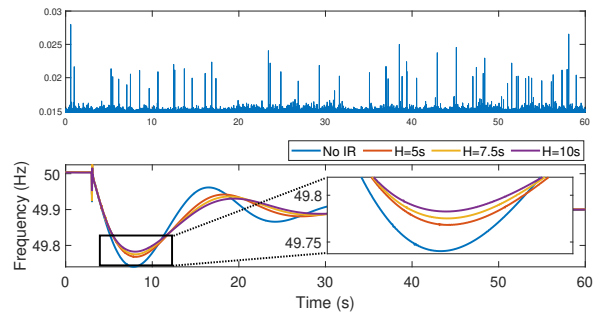
when the network is split at the border of Scotland and England (Subsystem 1 - two buses in the north representing Scottish load centres, Subsystem 2 - remainder of the four buses representing the English load centres as in Fig. 15). While synchronous and asynchronous coupling offer stability for the impedance ratio identified under the two time delays, i.e., $\sim 60\,$ms average and $\sim 75\,$ms maximum for EESL and $\sim 16\,$ms average and $\sim 28\,$ms maximum for RTLab, the evaluation in Section VI reveals better accuracy for synchronous coupling with DPSL-RTLab time delays.

The synhronous GDS setup for the frequency support study of transmission network is shown in Fig. 15. As detailed in Section II-A, the time stamped dq components of the voltage, along with phase are sent from DPSL to RTLab forming the feed-forward loop while the time-stamped dq components and phase of the currents are sent back from RTLab to DPSL. To evaluate the impact of provision of IR through controllable loads on the frequency of the network, a 1GW disturbance (loss of generator emulated by increase in load) is introduced in Subsystem 1. About 20 % of the load demand is assumed to be fast acting and controllable. Inertial response in fast acting controllable loads is incorporated based on swing equation referred to as swing equation based inertial response (SEBIR) [42]. The response of the network to the disturbance with and without IR is presented in Fig. 16 (bottom). Three different levels of inertial support are considered, i.e., $H = 5$ $H = 7.5\,$s and $H = 10\,$s. The frequency response of the network improves with incorporation of IR, with better response for higher value of H. This demonstrates the successful use of synchronous GDS for frequency control study within a transmission network.

An additional simulation with different rates of data exchange is undertaken to assess the impact of transmission rate. The results for four different transmission rates (1kHz, 2kHz, 3kHz and 4kHz) have been presented in Fig. 17. As can be observed, the rate of transmission does not impact the time delay. The jitter and variability in the delay remains in the same order of magnitude. With appropriate time delay compensation implemented, the errors in frequency response are negligible.

VIII. FUTURE OUTLOOK

While the detailed models developed in this paper and the consequent establishment of the boundaries of stability will further the understanding of the applicability of GDS and
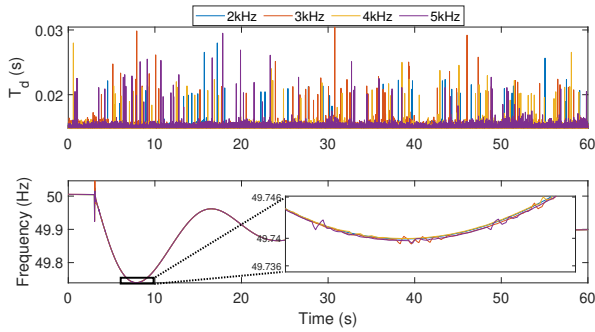
Fig. 17: Transmission rate impact assessment on synchronous GDS.

support safe implementations, there are still areas that present exciting directions for further exploration to support wide-scale adoption of the concept:

- As the concept of GDS becomes established, facilitated by adoption by research laboratories across the world, it becomes essential to maintain a database of such infrastructures and the services they offer. Furthermore, the business model or framework for collaborative use of the services needs to be explored. Most work to date is through bilateral research collaboration between research infrastructures, however commercialization opportunities can be explored.

- This work has presented the analysis of accuracy at a single PCC, i.e., in GDS implementation where the power network is split among two research infrastructures. For large scale implementations where the power network is split across more than two infrastructures, the transference of inaccuracies from one subsystem to the other requires further consideration and evaluation.

- Most research infrastructures undertaking GDS have reported custom implementations for the establishment of communications. A VPN tunnel is established between the two research infrastructures to facilitate secure transmission of data. A more standard approach to realization of communications is required to bolster wide scale adoption. One option for such secure and standardized approach is the development of service through cloud solutions platforms such as Amazon Web Services or Microsoft Azure.

IX. CONCLUSIONS

This paper presents small-signal stability models of GDS setups with two transformations, one for synchronous coupling (dq0) and one for asynchronous coupling (RMS). The derived models account for the transformation of interface signals, in addition to typical parameters of interest for stability analysis of geographically distributed simulations (GDS) setups. The proposed models have been verified through empirical simulation based analysis. Furthermore, boundaries of stable operation for synchronous and asynchronous GDS setups have been identified to establish their practical applicability. The boundaries are supplemented with accuracy analysis to enable informed decision on choice of coupling. Two case studies of GDS implementation for real-world smart grid applications have been presented, an asynchornous GDS for voltage control of dinstribution network between the Dynamic Power Systems Laboratory (DPSL) at the University of Strathclyde (Scotland)

and the Electric Energy Systems Laboratory at the National Technical University of Athens (Greece) and a synchronous GDS between DPSL and Real-Time Laboratory at RWTH Aachen (Germany). This thorough analysis will aid in understanding of the applicability of GDS and support its wide scale adoption that will enable the evaluation and subsequent realisation of experimental setups capable of encompassing the growing complexity of power systems. Future research directions to cater and support the growing interest in secure adoption of GDS have been identified.

REFERENCES

[1] J. Montoya *et al.*, "Advanced laboratory testing methods using real-time simulation and hardware-in-the-loop techniques: A survey of smart grid international research facility network activities," *Energies*, vol. 13, no. 12, 2020.

[2] A. Monti *et al.*, "A global real-time superlab: Enabling high penetration of power electron. in the electric grid," *IEEE Power Electron. Magazine*, vol. 5, no. 3, pp. 35–44, Sep. 2018.

[3] M. Syed *et al.*, "A Synchronous Reference Frame Interface for Geographically Distributed Real-Time Simulations," *IET GTD*, pp. 1–11, 2020.

[4] M. Stevic *et al.*, "Multi-site european framework for real-time co-simulation of power systems," *IET GTD*, vol. 11, no. 17, pp. 4126–4135, 2017.

[5] blackVogel, S. *et al.*, "Distributed Power Hardware-in-the-Loop Testing Using a Grid-Forming Converter as Power Interface," *Energies*, vol. 13, no. 15, p. 3770, Jul 2020.

[6] blackL. Pellegrino *et al.*, *Laboratory Coupling Approach*. Springer International Publishing, 2020, pp. 67–86.

[7] Y. Wang *et al.*, "A distributed control scheme of microgrids in energy internet and its multi-site implementation," *IEEE Trans. on Ind. Informatics*, vol. 66, no. 1, pp. 1–1, Feb 2020.

[8] black A. Avras *et al.*, "Development of a geographically distributed real-time test facility," *Journal of Physics: IOP Conference Series EERA DeepWind*, 2022.

[9] J. blackMontoya *et al.*, "Asynchronous integration of a real-time simulator to a geographically distributed controller through a co-simulation environment," in *IECON 2018 - 44th Annual Conference of the IEEE Industrial Electronics Society*, 2018, pp. 4013–4018.

[10] blackL. Pellegrino *et al.*, "Remote Laboratory Testing Demonstration," *Energies*, vol. 13, no. 9, p. 2283, May 2020.

[11] B. Palmintier *et al.*, "A power hardware-in-the-loop platform with remote distribution circuit cosimulation," *IEEE Trans. on Ind. Electron.*, vol. 62, no. 4, pp. 2236–2245, April 2015.

[12] S. Vogel *et al.*, "Improvements to the co-simulation interface for geographically distributed real-time simulationmulti-site european framework for real-time co-simulation of power systems," in *IECON 2019*, vol. 1, Oct 2019, pp. 6655–6662.

[13] B. Lundstrom *et al.*, "Trans-oceanic remote power hardware-in-the-loop: multi-site hardware, integrated controller, and electric network co-simulation," *IET GTD*, vol. 11, no. 18, pp. 4688–4701, 2017.

[14] M. H. Syed *et al.*, "Real-time coupling of geographically distributed research infrastructures: Taxonomy, overview, and real-world smart grid applications," *IEEE Trans. on Smart Grid*, pp. 1747–1760, 2021.

[15] A. Markou *et al.*, "Improving existing methods for stable and more accurate power hardware-in-the-loop experiments," in *2017 IEEE 26th International Symposium on Ind. Electron. (ISIE)*, 2017, pp. 496–502.

[16] Z. Feng *et al.*, "A scheme to improve the stability and accuracy of power hardware-in-the-loop simulation," in *IECON 2020 The 46th Annual Conference of the IEEE Industrial Electronics Society*, 2020.

[17] P. C. Kotsampopoulos *et al.*, "The limitations of digital simulation and the advantages of phil testing in studying distributed generation provision of ancillary services," *IEEE Trans. on Ind. Electron.*, vol. 62, no. 9, pp. 5502–5515, 2015.

[18] D. Barakos *et al.*, "Methods for stability and accuracy evaluation of power hardware in the loop simulations," in *MedPower 2014*, 2014, pp. 1–5.

[19] N. D. Marks *et al.*, "Stability of a switched mode power amplifier interface for power hardware-in-the-loop," *IEEE Trans. on Ind. Electron.*, vol. 65, no. 11, pp. 8445–8454, 2018.

[20] E. Guillo-Sansano *et al.*, "Assessment and development of stability enhancing methods for dynamically changing power hardware-in-the-loop simulations," in *CIRED 2019*, 2019, pp. 1–5.

[21] W. Ren *et al.*, "Improve the stability and the accuracy of power hardware-in-the-loop simulation by selecting appropriate interface algorithms," *IEEE Trans. on Industry Applications*, vol. 44, no. 4, pp. 1286–1294, 2008.

[22] R. Brandl, "Operational range of several interface algorithms for different power hardware-in-the-loop setups," *Energies*, vol. 10, no. 12, p. 1946, Nov 2017.

[23] E. Guillo-Sansano, *Novel methods for enhancing accuracy and stability of power hardware-in-the-loop simulations*. University of Strathclyde, 2018.

[24] M. Dargahi, *Stability Analysis and Implementation of Power-Hardware-in-the-Loop for Power System Testing*. Queensland University of Technology, 2015.

[25] P. Kotsampopoulos *et al.*, "A benchmark system for hardware-in-the-loop testing of distributed energy resources," *IEEE Power and Energy Technology Systems Journal*, vol. 5, no. 3, pp. 94–103, 2018.

[26] G. F. Lauss *et al.*, "Characteristics and design of power hardware-in-the-loop simulations for electrical power systems," *IEEE Trans. on Ind. Electron.*, vol. 63, no. 1, pp. 406–417, 2016.

[27] G. Lauss *et al.*, "Power hardware in the loop simulation with feedback current filtering for electric systems," in *IECON 2011 - 37th Annual Conference of the IEEE Ind. Electron. Society*, 2011, pp. 3725–3730.

[28] G. Lauss and K. Strunz, "Multirate partitioning interface for enhanced stability of power hardware-in-the-loop real-time simulation," *IEEE Trans. on Ind. Electron.*, vol. 66, no. 1, pp. 595–605, 2019.

[29] O. Tremblay *et al.*, "A multi-time-step transmission line interface for power hardware-in-the-loop simulators," *IEEE Trans. on Energy Conversion*, vol. 35, no. 1, pp. 539–548, 2020.

[30] K. Upamanyu and G. Narayanan, "Improved accuracy, modeling, and stability analysis of power-hardware-in-loop simulation with open-loop inverter as power amplifier," *IEEE Trans. on Ind. Electron.*, vol. 67, no. 1, pp. 369–378, 2020.

[31] G. Lauss and K. Strunz, "Accurate and stable hardware-in-the-loop (hil) real-time simulation of integrated power electron. and power systems," *IEEE Trans. on Power Electron.*, vol. 36, no. 9, pp. 10 920–10 932, 2021.

[32] M. Dargahi *et al.*, "Stability synthesis of power hardware-in-the-loop (phil) simulation," in *2014 IEEE PES General Meeting — Conference Exposition*, 2014, pp. 1–5.

[33] E. Guillo-Sansano *et al.*, "Harmonic-by-harmonic time delay compensation method for phil simulation of low impedance power systems," *2015 International Symposium on Smart Electric Distribution Systems and Technologies (EDST)*, pp. 560–565, 2015.

[34] Z. Feng *et al.*, "Interface compensation for more accurate power transfer and signal synchronization within power hardware-in-the-loop simulation," in *IECON 2021 The 47th Annual Conference of the IEEE Industrial Electronics Society*, 2021.

[35] A. Riccobono *et al.*, "Online parametric identification of power impedances to improve stability and accuracy of power hardware-in-the-loop simulations," *IEEE Trans. on Instrum. Meas.*, vol. 66, no. 9, pp. 2247–2257, 2017.

[36] J. Langston *et al.*, "Practical estimation of accuracy in power hardware-in-the-loop simulation using impedance measurements," *IEEE Trans. on Power Systems*, vol. 36, no. 3, pp. 2584–2593, 2021.

[37] B. Lundstrom and M. Salapaka, "Optimal power hardware-in-the-loop interfacing: Applying modern control for design and verification of high-accuracy interfaces," *IEEE Trans. on Ind. Electron.*, pp. 1–1, 2020.

[38] S. Chattopadhyay, M. Mitra, and S. Sengupta, "Clarke and park transform," in *Electric Power Quality*. Springer, 2011, pp. 89–96.

[39] E. blackGuillo Sansano *et al.*, "Characterization of time delay in power hardware in the loop setups," *IEEE Transactions on Industrial Electronics*, vol. 68, no. 3, pp. 2703–2713, 2021.

[40] S. Pugliese, Y. Kwon, and M. Liserre, "Positive-Negative Sequence SRF-PLL Model for Accurate Stability Analysis in Grid-Tied Converters," in *IEEE Energy Conversion Congress and Exposition (ECCE)*, Oct. 2020.

[41] T. T. blackHoang, Q. T. Tran, and Y. Besanger, "An advanced protection scheme for medium-voltage distribution networks containing low-voltage microgrids with high penetration of photovoltaic systems," *International Journal of Electrical Power & Energy Systems*, vol. 139, p. 107988, 2022.

[42] blackM. Yu *et al.*, "Effects of swing equation-based inertial response (sebir) control on penetration limits of non-synchronous generation in the gb power system," in *International Conference on Renewable Power Generation (RPG 2015)*, Oct 2015, pp. 1–6.

Mazheruddin Syed (S'11-M'18) received his BE degree in Electrical and Electronics Engineering from Osmania University, India, in 2011, MSc degree in Electrical Power Engineering from Masdar Institute of Science and Technology, UAE, in 2013 and PhD degree in Electronic and Electrical Engineering from University of Strathclyde, Scotland in 2018. He is currently a Strathclyde Chancellor's Fellow (Lecturer) with the Institute for Energy and Environment in the Department of Electronic and Electrical Engineering at the University of Strathclyde. He also serves as the manager for the Dynamic Power Systems Laboratory at Strathclyde. He leads the International Energy Agency (IEA) ISGAN SIRFN Advanced Laboratory Testing Methods Task and is the Secretary of IEEE Task Force on Control of Distributed Resources in Energy Internet. He has lead and contributed to innovative National, European and Industrial power system research projects with a strong publication record of over 62 peer-reviewed scientific papers. His research interests include demand side management, decentralized and distributed control, real-time controller and power hardware in the loop simulations, geographically distributed simulations and systems level validations.

Tran The Hoang received his B.Sc and M.Sc degrees in Electrical Engineering in 2010 and 2012, respectively from Tomsk Polytechnic University, Russia, and PhD degree from G2Elab, Grenoble Institute of Technology, France in 2020. From 2012 to 2017, he worked as a lecturer and researcher at the Danang University of Science and Technology, Vietnam. From 2020 to 07/2022 he was with the National Institute of Solar Energy, French Alternative Energies and Atomic Energy Commission, France. Since 08/2022 he has been working as a Research Fellow at the Department of Electrical, Computer, and Software Engineering, the University of Auckland, New Zealand where he is mainly involved in the Future Architecture of the Network (FAN) project or Te Whatunga Hiko granted by the New Zealand government's Strategic Science Investment Fund. His interest of research includes adaptive protection, fault location, real time simulation and its stability, and IEC 61850-based digital substation. He has been serving as a reviewer for IEEE, Elsevier, and Frontier journals.
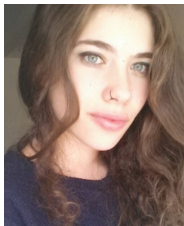
Alkistis C. Kontou (S'22) received the Diploma degree in Electrical and Computer Engineering from the National Technical University of Athens, Greece, in 2019. During 2019 she was also an intern with BayWa r.e, Berlin. Since 2019, she has been a PhD Candidate and works as a Researcher within the Department of Electrical and Computer Engineering in National Technical University of Athens, Greece. Her research interests lie in control of power inverters, converter-driven stability, microgrids, cyber-security aspects of smart grids and laboratory validation methods. She has contributed to several European and national research projects in the field of power systems. She is a Student Member of the IEEE and a Member of the Technical Chamber of Greece.

Alexandros G. Paspatis (M'12) received the Diploma degree in electrical and computer engineering from the Democritus University of Thrace, Komotini, Greece, in 2016, and the Ph.D. degree in automatic control and systems engineering from the Department of Automatic Control and Systems Engineering, The University of Sheffield, Sheffield, U.K., in 2020. In 2018, he was a Research Assistant with the Department of Automatic Control and Systems Engineering, The University of Sheffield. Since 2020, he has been with the School of Electrical and Computer Engineering, National Technical University of Athens, Athens, Greece, as a Postdoctoral Research Associate and the Department of Electrical and Computer Engineering, Hellenic Mediterranean University, Heraklion, Greece, as an Adjunct Lecturer. His research interests lie in control of power inverters, converter-driven stability, microgrids and laboratory validation methods. He has contributed to several European and national research and industrial projects in the field of power systems. Dr. Paspatis is a Member of IEEE, a member of IEEE Task Forces and a Member of the Technical Chamber of Greece. Moreover, he acts as a regular reviewer for IEEE, Elsevier and MDPI journals and has been a Guest Editor for Applied System Innovation.

Graeme M. Burt (M'95) received the B.Eng. degree in electrical and electronic engineering, and the Ph.D. degree in fault diagnostics in power system networks from the University of Strathclyde, Glasgow, U.K., in 1988 and 1992, respectively. He is a distinguished professor of electrical power systems in the Department of Electronic and Electrical Engineering at the University of Strathclyde, UK, where he directs the Institute for Energy and Environment. His research interests span decentralised and hybrid energy systems, electrification of propulsion, and experimental validation of advanced power systems. Professor Burt is lead academic for the PNDC, a MW-scale innovation and testing infrastructure, and director of the Rolls-Royce UTC (University of Strathclyde, Glasgow) in Electrical Power Systems. He also serves as the Theme Lead in power systems and grid technologies for Scotland's Energy Technology Partnership. He is an active researcher, with a track record of leading involvement in many national and international power systems consortia research projects and professional activities (such as the CIRED WG for DC Distribution Networks), and an extensive track record of publication. Professor Burt also serves on the Steering Committee of the European Energy Research Alliance (EERA) Joint Programme in Smart Grids, the Scientific Advisory Body of the Clean Aviation Joint Undertaking, and the Board of the Association of European Distributed Energy Resources Laboratories (DERlab e.V.).

Quoc Tuan Tran received his Ph.D. degree in Electrical Engineering from the Grenoble Institute of Technology in 1993. He is currently a Professor with INSTN – Paris Saclay University, and a Scientific Manager with Alternative Energies and Atomic Energy Commission (CEA) - National Institute for Solar Energy (INES). His research interests are in the fields of power system analysis, operations, electromagnetic transients, distributed generation, smart grid and renewable energy. He is an IEEE senior member.

Steffen Vogel received his B.Sc. and M.Sc. degrees in electrical engineering, information technology, and computer engineering in 2014 and 2017, respectively, both from RWTH Aachen University, Germany. Currently, he is a researcher at the Institute for Automation of Complex Power Systems, Rheinisch-Westfälische Technische Hochschule Aachen University, Aachen, Germany.

Ha Thi Nguyen received the Ph. D. degree in electric power systems from Technical University of Denmark (DTU), Denmark in 2018. She has worked as a Visiting Scholar at the Center Energy Research - University of California, San Diego, a Postdoc at Electric Power and Energy Center – DTU, and Lecturer at Danang University of Science and Technology. She is currently an Assistant Research Professor at Eversource Energy Center – Department of Electrical and Computer Engineering - University of Connecticut (UConn), where she leads the real-time digital simulator (RTDS) power grid testbed and supports research projects related to the integration of renewables in the power grid, cybersecurity, power system protection and power system resilience. Her research interests include power system modelling, operation, control and protection, frequency stability and control for low-inertia systems, renewable energy integration, and geographically distributed power-hardware-in-the-loop simulation, and cyber-physical security.

Nikos D. Hatziargyriou is with the National Technical University of Athens (NTUA), since 1984, professor in Power Systems, since 1995, and Professor Emeritus, since February 2022. He is Part-time Professor at the University of Vaasa, Finland. He has over 10 year industrial experience as Chairman and CEO of the Hellenic Distribution Network Operator (HEDNO) and as executive Vice-Chair and Deputy CEO of the Public Power Corporation (PPC), responsible for the Transmission and Distribution Divisions. He was chair and vice-chair of the EU Technology and Innovation Platform on Smart Networks for Energy Transition (ETIP-SNET). He is honorary member of CIGRE and past Chair of CIGRE SC C6 "Distribution Systems and Distributed Generation". He is Life Fellow Member of IEEE, past Chair of the Power System Dynamic Performance Committee (PSDPC) and past Editor in Chief (EiC) of the IEEE Trans on Power Systems, currently EiC at Large for PES Transactions. He is the 2017 recipient of the IEEE/PES Prabha S. Kundur Power System Dynamics and Control Award and the 2023 recipient of the IEEE Herman Halperin Electric Transmission and Distribution Award. He has participated in more than 60 RDD projects funded by the EU Commission, electric utilities and industry for fundamental research and practical applications. He is author of the book "Microgrids: Architectures and Control" and of more than 300 journal publications and 600 conference proceedings papers. He is included in the 2016, 2017 and 2019 Thomson Reuters lists of the top 1% most cited researchers and he is 2020 Globe Energy Prize laureate.